



Title	Structural and magnetic properties of Ni78Fe22 thin films sandwiched between low-softening-point glasses and application in spin devices
Author(s)	Misawa, Takahiro; Mori, Sumito; Komine, Takashi; Fujioka, Masaya; Nishii, Junji; Kaiju, Hideo
Citation	Applied surface science, 390, 666-674 <a href="https://doi.org/10.1016/j.apsusc.2016.08.100">https://doi.org/10.1016/j.apsusc.2016.08.100</a>
Issue Date	2016-12-30
Doc URL	<a href="http://hdl.handle.net/2115/72258">http://hdl.handle.net/2115/72258</a>
Rights	(C) 2016 Elsevier B.V. All rights reserved.
Rights(URL)	<a href="http://creativecommons.org/licenses/by-nc-nd/4.0/">http://creativecommons.org/licenses/by-nc-nd/4.0/</a>
Type	article (author version)
File Information	ASS-2016-Kaiju.pdf



[Instructions for use](#)

# Structural and magnetic properties of Ni<sub>78</sub>Fe<sub>22</sub> thin films sandwiched between low-softening-point glasses and application in spin devices

Takahiro Misawa<sup>a</sup>, Sumito Mori<sup>a</sup>, Takashi Komine<sup>b</sup>, Masaya Fujioka<sup>a</sup>,  
Junji Nishii<sup>a</sup>, Hideo Kaiju<sup>a,\*</sup>

<sup>a</sup>*Research Institute for Electronic Science, Hokkaido University, Sapporo, Hokkaido 001-0020, Japan*

<sup>b</sup>*Faculty of Engineering, Ibaraki University, Hitachi, Ibaraki 316-8511, Japan*

## ABSTRACT

We investigate the structural and magnetic properties of Ni<sub>78</sub>Fe<sub>22</sub> thin films sandwiched between low-softening-point (LSP) glasses, which can be used in spin quantum cross (SQC) devices utilizing stray magnetic fields generated from magnetic thin-film edges. We also calculate the stray magnetic field generated between the two edges of Ni<sub>78</sub>Fe<sub>22</sub> thin-film electrodes in SQC devices and discuss the applicability to spin-filter devices. Using the established fabrication technique, we successfully demonstrate the formation of LSP-glass/Ni<sub>78</sub>Fe<sub>22</sub>/LSP-glass structures with smooth and clear interfaces. The coercivity of the Ni<sub>78</sub>Fe<sub>22</sub> thin films is enhanced from 0.9 to 103 Oe by increasing the applied pressure from 0 to 1.0 MPa in the thermal pressing process. According to the random anisotropy model, the enhancement of the coercivity is attributed to the increase in the crystal grain size. The stray magnetic field is also uniformly generated from the Ni<sub>78</sub>Fe<sub>22</sub> thin-film edge in the direction perpendicular to the cross section of the LSP-glass/Ni<sub>78</sub>Fe<sub>22</sub>/LSP-glass structures. Theoretical calculation reveals that a high stray field of approximately 5 kOe is generated when the distance between two edges of the Ni<sub>78</sub>Fe<sub>22</sub> thin-film electrodes is less than 5 nm and the

thickness of Ni<sub>78</sub>Fe<sub>22</sub> is greater than 20 nm. These experimental and calculation results indicate that Ni<sub>78</sub>Fe<sub>22</sub> thin films sandwiched between LSP glasses are useful as electrodes for SQC devices, serving as spin-filter devices.

*Keywords:*

Magnetic thin films, thermal pressing, coercivity, spin filter, micromagnetic simulation.

\* Corresponding author.

*E-mail address:* [kaiju@es.hokudai.ac.jp](mailto:kaiju@es.hokudai.ac.jp) (H. Kaiju).

## 1. Introduction

Spintronics has received much attention owing to the fascinating phenomena that provide new functionalities in conventional electronic devices [1–10]. One of the most attractive phenomena in spintronics is the spin-filter effect, wherein a highly spin-polarized current can be generated from nonmagnetic electrodes via tunnel barriers [6–10]. The spin-filter effect has been observed in two metal electrodes separated by a ferromagnetic tunnel barrier such as EuS [6,7], EuSe [8], and BiMnO<sub>3</sub> [9]. In this device, two different barrier heights are created by the exchange splitting of the energy levels in the conduction band of the tunnel barrier, yielding a highly spin-polarized current. Another example is based on the Rashba effect in multi-layered semiconductor devices comprising three tunnel barriers and two quantum wells [10]. The Rashba effect in this system can induce spin-split resonant tunneling levels, which give rise to the spin selectivity of the tunnel current by applying a bias voltage.

Recently, we proposed spin quantum cross (SQC) devices, which comprise inorganic complexes or quantum dots (QDs) sandwiched between two edges of magnetic thin-film electrodes with their edges crossed, towards the realization of novel spin-filter devices [11,12]. In the SQC devices, the junction area is determined by the film thickness; that is, 10–100-nm-thick films could produce 10×10–100×100-nm<sup>2</sup> nanoscale junctions. In addition to this feature, a high magnetic field is induced in the inorganic complexes or QDs between the two film edges owing to the generation of a strong stray field from both edges. This high magnetic field produces a large Zeeman effect, which enhances the energy splitting of the inorganic complexes or QDs. Therefore, a large spin-filter effect can be expected.

In a previous study, towards the creation of SQC devices, we investigated the structural and magnetic properties of Co thin films on low-softening-point (LSP) glasses and Co thin films sandwiched between LSP glasses, which can be used in the electrodes of SQC devices [12]. As a result of the establishment of the fabrication technique, we successfully demonstrated the formation of smooth Co thin films and flat Co edges along with the generation of stray magnetic fields from Co edges. This technique can also be applied to other ferromagnetic materials such as Fe and Ni. Particularly, NiFe alloy is an excellent material for magnetic electrodes of spintronic devices or magnetic soft/hard materials due to its large magnetization, high controllability of spin transports, and long-term stability in air [13–17]. In this study, we investigate the structural and magnetic properties of Ni<sub>78</sub>Fe<sub>22</sub> thin films on LSP glasses and Ni<sub>78</sub>Fe<sub>22</sub> thin films sandwiched between LSP glasses used in SQC devices. We also calculate the stray magnetic field generated between the two edges of Ni<sub>78</sub>Fe<sub>22</sub> thin-film electrodes in SQC devices using micromagnetic simulation and discuss the applicability to spin-filter devices.

## 2. Experimental

Ni<sub>78</sub>Fe<sub>22</sub> (permalloy, Py in the following) thin films were deposited on B<sub>2</sub>O<sub>3</sub>-based LSP glasses with a glass transition temperature  $T_g$  of 464°C (ISUZU GLASS CO., LTD.) under an in-plane magnetic field of 400 Oe by ion beam sputtering. The dimensions of the LSP glasses were 10×10×2 mm<sup>3</sup>. The base pressure before sputtering was 1.0–5.0×10<sup>-5</sup> Pa, and the growth rate of Py thin films was 3 nm/min at a sputtering power of 60 W (1.0 kV and 60 mA) under an

Ar pressure of  $3.0\text{--}4.5\times 10^{-2}$  Pa. The Py thin films sandwiched between the LSP glasses were then fabricated using a thermal pressing technique. This technique is based on a glass-molding machine (Toshiba Machine Co. Ltd., GMP-00504V). The sputtered Py thin film on the LSP glass was placed on the sample stage inside the machine, and the LSP glass with the same composition was stacked on this sample. The stacked sample was heated up to  $513^{\circ}\text{C}$  ( $10^{\circ}\text{C}$  higher than the temperature of glass deformation) at  $2.5^{\circ}\text{C/s}$  in  $\text{N}_2$  atmosphere, and kept for 30 s. Then, the sample was pressed at  $0.25\text{--}1.0$  MPa for 5 min. After the pressing operation, the pressure was released and cooled down to room temperature at  $1^{\circ}\text{C/s}$ . Finally, the cross-sectional surfaces of the stacked samples were polished by a mechanical polishing method using  $\text{Al}_2\text{O}_3$ -based emeries and a chemical mechanical polishing method using  $\text{Al}_2\text{O}_3$  and  $\text{SiO}_2$  slurries.

The surface morphologies and roughnesses of the samples were analyzed using atomic force microscopy (AFM; SII Nano Technology Inc., Nanocute). The microstructures and interfacial structures of the samples were examined using transmission electron microscopy (TEM; JEOL, JEM-ARM200F) and transmission electron diffraction (TED) operating at 200 kV. The cross-sectional TEM specimens were prepared by a focused ion beam (FIB; Hitachi High-Tech. Corp., FB-2100) system. The crystal grain sizes of the Py thin films were determined by X-ray diffraction (XRD; Rigaku, SmartLab). The magnetization curves were measured by focused magneto-optical Kerr effect (MOKE; NEOARK, BH-PI920-HU) under a magnetic field of up to 1 kOe at room temperature. The stray fields originating from the edges of Py thin films were observed using magnetic force microscopy (MFM), in which a

CoCrPt-coated cantilever (Si-MF20) was used in the AFM setup described above. The local magnetic fields generated between the two edges of Py thin-film electrodes in SQC devices were calculated using micromagnetic simulation. The calculation region was semi-infinite space corresponding to SQC devices, and the region was divided into  $0.1 \times 0.1 \times 0.1 \text{ nm}^3$  cubic mesh. The stray field computation was carried out by using demagnetization tensor and numerical integration. Fortunately, the demagnetization coefficient of SQC is approximately zero. Since the magnetization in SQC almost orients to the transverse direction of the films, the stray field was obtained from the most contribution due to magnetic charges at the film edges.

### **3. Results and discussion**

#### *3.1. $\text{Ni}_{78}\text{Fe}_{22}$ thin films on LSP glasses*

Fig. 1a and b shows the cross-sectional bright-field TEM images of Py thin films with thicknesses of 17 and 86 nm on LSP glasses, which are denoted by Py17 and Py86, respectively (integer numbers are the Py layer thicknesses in nm). There was no diffusion of Ni and Fe atoms into the LSP glass, resulting in the formation of a clear interface between Py thin films and LSP glasses and smooth Py thin-film surfaces. Some researchers have pointed out that metal atoms diffuse into LSP materials in the process of metal deposition onto LSP materials [18,19]. For example, a cross-sectional TEM observation of the interface between Au and polymethyl methacrylate (PMMA) prepared by dip-coating demonstrated that the thickness of the interfacial region ranges from 2 to 4 nm. This means that Au atoms diffuse into PMMA layers [18]. In another study, radiotracer measurements in conjunction with

ion-beam depth profiling of Ag/trimethylcyclohexane polycarbonate (TMC-PC) revealed that traces of Ag atoms can be detected in TMC-PC at a depth of 400 nm [19]. In contrast to the above results, such metal diffusion into LSP materials did not occur at the Py/LSP interface in this study. This means that Py thin films on LSP glasses are good candidates for electrodes of SQC devices. The high-resolution cross-sectional TEM images of the same specimens are shown in Fig. 1c and d. Py thin films on LSP glasses have polycrystalline structures with nanosized grains. A detailed discussion of the grain sizes of Py thin films is given in the next section.

Fig. 2a shows the dependence of the root mean square (RMS) surface roughness ( $R_q$ ) on the thickness of the Py thin film on LSP glass. The  $R_q$  values of Py thin films evaporated on polyethylene naphthalate (PEN), which have been already examined as the magnetic thin-film electrodes of SQC devices [20], is also plotted. The insets show the surface AFM images of an LSP glass, Py17, and Py86. The scanning area was  $500 \times 500 \text{ nm}^2$ . The  $R_q$  values were investigated in randomly selected 10 areas at each Py thickness, and the average value in these areas is plotted in Fig. 2a. As can be seen in this figure, the  $R_q$  values of Py thin films on LSP glasses (0.73–0.88 nm) are smaller than those of Py thin films on PEN (1.65–1.68 nm) and are also almost similar to or slightly smaller than those of Co thin films on LSP glasses (0.87–1.2 nm)[12]. The smooth surfaces of the Py thin films on LSP glasses are consistent with the TEM results shown in Fig. 1. Fig. 2b shows the scaling properties of  $R_q$  for an LSP glass and Py thin films on LSP glasses.  $R_q$  obeys a scaling law,  $R_q = w(L) \propto L^\alpha$ , where  $w(L)$  is the interface width, which corresponds to the standard deviation of the surface height;  $L$  is the system size;

and  $\alpha$  is the growth scaling exponent. The value of  $\alpha$  remains almost constant at 0.59–0.61 for LSP glass and Py thin films on LSP glasses, as indicated by the similar roughness slope for each sample. This means that the surface morphologies of Py thin films on LSP glasses are independent of film thickness and exhibit the same behavior as an LSP glass, which is consistent with the surface AFM images in the inset of Fig. 2a. We also note that the surface can be described by a self-affine structure due to  $\alpha \neq \beta$ , where  $\beta$  is the dynamical exponent in the scaling law  $R_q = w(t) \propto t^\beta$ . Here,  $t$  is a film thickness. As can be seen in Fig. 2a, the dynamical exponent  $\beta$  of Py thin films on LSP glasses is nearly equal to zero because  $R_q$  is almost the same at each Py thickness. This results in  $\alpha \neq \beta$ , indicating a self-affine growth regime, which can be observed in evaporated Py thin films on PEN and sputtered Cu films on glasses [20,21]. Here, we discuss the application of Py thin films to SQC devices from the viewpoint of surface roughness. As described in the introduction, the junction area of an SQC device is determined by the film thickness. Therefore, the surface roughness must be sufficiently small at a scanning scale equal to the film thickness. As shown in Fig. 2b, at a scanning scale of 9 nm, the surface roughnesses of Py9 and the LSP glass are as small as 0.11 and 0.07 nm, respectively, corresponding to a few atomic layers. The surface roughness of Py86 is less than 0.5 nm at a scanning scale equal to the Py thickness. These results indicate that Py thin films on LSP glasses are useful as electrodes for SQC devices from the perspective of surface morphologies as well as interfacial structures.

Fig. 3 shows the magnetization curves for Py17 and Py86 measured using the MOKE technique. The magnetic field was applied in the  $x$  and  $z$  directions, which correspond to the magnetic easy- and hard-axis directions, respectively. Magnetic anisotropy was induced in both of the Py thin films. The coercivity of Py17 was as low as 0.9 Oe, which is almost the same as the typical value for Py films [17]. The squareness of the hysteresis loop  $M_r/M_s$ , where  $M_r$  and  $M_s$  are the remanent and saturation magnetizations, respectively, was as large as 0.99. Similar magnetic behavior was also observed in Py86, for which the coercivity was 1.1 Oe, and the squareness was 0.98. These results indicate that high-quality Py thin films can be formed on LSP glasses from the viewpoint of magnetic properties.

### 3.2. $Ni_{78}Fe_{22}$ thin films sandwiched between LSP glasses

Fig. 4a and b shows the cross-sectional TEM images of Py thin films sandwiched between LSP glasses after thermal pressing at 1.0 MPa, which are denoted by s-Py13 and s-Py78, respectively. The thicknesses of the Py thin films before thermal pressing were 17 and 86 nm, respectively. The TEM images indicated that the thicknesses of s-Py13 and s-Py78 decreased to 13 and 78 nm, respectively, after thermal pressing. Here, we emphasize that we successfully demonstrated the formation of LSP-glass/Py/LSP-glass structures with smooth and clear interfaces; that is, there was no diffusion of Fe and Ni atoms into the LSP glasses. This is an important result because it allows for the formation of nanolines and flat edge surfaces, leading to the creation of nanoscale junctions in SQC devices. The high-resolution cross-sectional TEM images of s-Py13 and s-Py78 are shown in Fig. 4c and d, respectively. The s-Py13

sample exhibited a highly oriented crystalline structure. On the other hand, a polycrystalline structure with a grain size of  $\sim 10$  nm was observed in s-Py78. A detailed discussion on grain sizes is given later in this section. Here, we focus on the thickness change of the Py thin films after thermal pressing. The volume of 17-nm-thick Py films was changed from  $8.28 \text{ mm} \times 9.99 \text{ mm} \times 17 \text{ nm}$  to  $8.64 \text{ mm} \times 11.05 \text{ mm} \times 13 \text{ nm}$  after the thermal pressing. This corresponds to a 12% decrease in volume. The volume of 86-nm-thick Py films was also changed from  $8.38 \text{ mm} \times 10.18 \text{ mm} \times 86 \text{ nm}$  to  $8.54 \text{ mm} \times 10.98 \text{ mm} \times 78 \text{ nm}$ . This corresponds to a 0.3% decrease in volume. These results indicate that the volume change of thinner films is more likely to be affected by the thermal pressing than that of thick films. These volume changes are attributed to the crystallinity in Py films. As described above, the crystal grain size increases after the pressing. This means the reduction of the grain boundary area, contributing to the decrease in volume. We also note that the films elongate in the direction perpendicular to the pressing axis. This film change is considered to give an influence on the interfacial region; the shear can be applied to the Py films near the Py/LSP interfacial region by elongating the Py film, and this shear stress gives an influence on the crystal growth of Py near the interfacial region. This is consistent with the fact that there is a significant volume change for thinner samples.

Fig. 5 shows the magnetization curves of s-Py13 and s-Py78, which are the same specimens shown in Fig. 4. The magnetic field was applied in the  $x$  and  $z$  directions, as shown in the inset of Fig. 5. The magnetization curves of the samples after thermal pressing drastically changed compared to those of Py thin films before thermal pressing (Fig. 3). The magnetic anisotropy vanished, and the coercivity increased in the samples after thermal pressing. Specifically, the

coercivity was enhanced from 0.9 to 103 Oe for s-Py13 and from 1.1 to 24 Oe for s-Py78. Fig. 6 shows the pressure dependence of the coercivity for Py thin films sandwiched between LSP glasses. The thicknesses of Py thin films before thermal pressing were 17, 42, and 86 nm. The coercivity increased proportionally with applied pressure for each sample, and a remarkable increase in coercivity was observed in the thinner Py films.

In order to clarify the origin of the coercivity enhancement, we investigated the structural properties of the Py thin films before and after thermal pressing. Fig. 7a and b show the TED patterns for Py17 and Py86. The TED patterns of both samples were obtained with a beam size of 100 nm and exhibit ring shapes. These ring patterns indicate the formation of polycrystalline structures with fine grains, which is consistent with the TEM images shown in Fig. 1c and d. Fig. 7c and d shows the TED patterns for s-Py13 and s-Py78, respectively, after thermal pressing at 1.0 MPa. The TED patterns of both samples show clear spots, indicating that the number of grains decreased (i.e., the crystal grain size increased). Since the ring patterns were not observed in the probing area (~100 nm) for s-Py13, we concluded that the crystal grain size increased to ~100 nm in this sample after thermal pressing. This is consistent with the highly oriented crystalline structures observed in Fig. 4c. To obtain a quantitative understanding of the grain size, we carried out XRD measurements on Ni<sub>78</sub>Fe<sub>22</sub> thin films. Because the XRD signal is weak in Py17, the measurement was carried out in Py86. Fig. 8 shows the XRD spectra of Py86 before and after thermal pressing at 1.0 MPa. The average crystal grain size in Py thin films can be estimated using Scherrer's equation from the full width at half maximum of the peak in the XRD spectrum. Table 1 shows the average crystal grain sizes in the (111), (200),

and (220) planes estimated by Scherrer's equation. The average crystal grain size increased by 2.1–3.4 times in each plane after thermal pressing. This finding is consistent with the TEM images in Fig. 1d and 4d and the TED patterns in Fig. 7b and d. We now discuss the relationship between grain size and coercivity in Py thin films. The dependence of the coercivity on grain size in magnetic *bulk* materials with nanocrystalline structures can be explained by theoretical calculation based on the three-dimensional (3D) random anisotropy model [22,23]. This model can be extended to the case of magnetic *thin films* with nanocrystalline structures. In the extended model, the nanosized grains with magnetocrystalline anisotropies  $K_1$ , which are randomly oriented, are ferromagnetically coupled in the two-dimensional (2D) magnetic system. The ferromagnetic exchange length  $L_{\text{ex}}$  of this system is given by

$$L_{\text{ex}} = \left( \frac{A}{\langle K \rangle} \right)^{\frac{1}{2}}, \quad (1)$$

where  $A$  is the exchange stiffness constant, and  $\langle K \rangle$  is the anisotropy energy density. Since  $\langle K \rangle$  indicates the mean fluctuation amplitude of the anisotropy energy of  $N (= (L_{\text{ex}}/l_g)^2)$  grains, where  $l_g$  is the crystal grain size,  $\langle K \rangle$  can be expressed by

$$\langle K \rangle = \frac{K_1}{\sqrt{N}} = \frac{K_1 l_g}{L_{\text{ex}}}. \quad (2)$$

Substituting Eq. (1) in Eq. (2) yields  $\langle K \rangle = K_1^2 l_g^2 / A$ . Therefore, the coercivity is represented by

$$H_c = \frac{2K_1^2 l_g^2}{M_s A}, \quad (3)$$

where  $M_s$  is the saturated magnetization. Eq. (3) indicates that the coercivity increases proportionally with  $l_g^2$ . As shown in Fig. 3a and 5a, the coercivity of Py17 was enhanced from 0.9 to 103 Oe after thermal pressing. In this sample, the grain size was considered to have increased from 8.5 to ~100 nm after thermal pressing based on the above-mentioned XRD and TED results. This change corresponds to a coercivity enhancement of two orders of magnitude for a grain size enhancement of one order of magnitude. This result is consistent with Eq. (3) (i.e.,  $H_c \propto l_g^2$ ). This interpretation can also be applied to the case of Py86. As shown in Fig. 3b and 5b, the coercivity of this sample was enhanced from 1 to 24 Oe after thermal pressing, and the grain size increased from 8.5 to 17.8 nm (Table 1). Therefore, the relationship between coercivity and grain size was described by  $H_c \propto l_g^{4.3}$ . According to the 3D random anisotropy model, the coercivity in magnetic *bulk* materials is given by  $H_c \propto l_g^6$ . Because 86-nm-thick films are regarded as materials between 2D and 3D systems, it is reasonable that the exponent  $\gamma$  in  $H_c \propto l_g^\gamma$  is 4.3 because  $2 < \gamma < 6$ . In summary, these results suggest that the enhancement in coercivity after thermal pressing can be attributed to the increase in crystal grain size with random magnetic anisotropy.

Fig. 9a and b show the AFM images of polished cross-sectional surfaces of s-Py13 and s-Py78. Py thin-film edges can be confirmed at the centers of the samples. The roughnesses in scanning areas of  $500 \times 500 \text{ nm}^2$  of the polished surfaces were as small as 0.42 and 1.2 nm for the samples with thicknesses of 13 and 78 nm, respectively. The  $R_q$  of the polished surface of s-Py13 (0.42 nm) is almost the same as that of s-Co14 (0.44 nm) [12]. Although the Py thin-film edges are convex upward ( $\sim$ nm), this edge structure enables a good contact between the Py edges and sandwiched materials in the junction of SQC devices. Fig. 9c and d show the MFM images of the same specimens shown in Fig. 9a and b, respectively. The stray magnetic field was generated along the out-of-plane direction from the Py thin-film edges. This stray field makes it possible to generate a local field between the two film edges in SQC devices. These results indicate that Py thin films sandwiched between LSP glasses can be used in electrodes of SQC devices from the viewpoint of structural and magnetic properties. Here, we discuss the influence of the chemical mechanical polishing method on the structural and magnetic properties for a prospective use of SQC devices. For the polishing in air (atmospheric pressure), there is a possibility of the oxidation of Py edge surfaces and it can provide a significant influence on the structural and magnetic properties in SQC devices. The chemical reactions include oxidation of Ni to form a NiO layer on the edge surface. Other reaction products, related to Fe, include the formation of  $\alpha$ -Fe<sub>2</sub>O<sub>3</sub>,  $\gamma$ -Fe<sub>2</sub>O<sub>3</sub> and Fe<sub>3</sub>O<sub>4</sub>. Since NiO and  $\alpha$ -Fe<sub>2</sub>O<sub>3</sub> are antiferromagnetic and  $\gamma$ -Fe<sub>2</sub>O<sub>3</sub> and Fe<sub>3</sub>O<sub>4</sub> are ferrimagnetic at room temperature, these formations cause the reduction of magnetization in Py edges and a weaker stray field can be generated from the edges. This results in a small spin filter effect in SQC devices. From a

perspective of such structural and magnetic properties, the investigation of the Py edge surface is of great importance for obtaining a large spin filter effect. If the perfect Py edge surface was not obtained in only the wet process, a dry process, such as ion etching in vacuum, could also be useful for the removal of the oxide layer in the final process of the edge treatment, which leads to the observation of a large spin filter effect.

### 3.3. Calculation of the stray magnetic field in SQC devices

Finally, we show the calculation results of the stray field generated between the two edges of Py electrodes in SQC devices and discuss the applicability of using Py electrodes in spin-filter devices. Fig. 10a shows the structure of an SQC device for calculating the stray field generated between the two edges of Py electrodes. The magnetization of Py was set to 859 emu/cc. The Py thickness  $t_{y(z)}$  was 5–20 nm, and the distance between the two edges of the Py electrode  $d$  was 5–20 nm. The origin of the  $(x, y, z)$  coordinates was chosen in the center of the junction. Fig. 10b–d shows the calculation results of the stray field at  $z = 0$  nm. For  $t_{y(z)} = 5$  and 20 nm at  $d = 20$  nm, showing in Fig. 10b and c, the stray field was low (2–4 kOe), and a uniform distribution was not obtained. In contrast, as shown in Fig. 10d, the stray field measured as high as 5 kOe, and a uniform distribution was successfully obtained for  $t_{y(z)} = 20$  nm and  $d = 5$  nm. Fig. 10e shows the stray field in the center of the junction as a function of Py thickness. This figure indicates that a high stray field of around 5 kOe was generated when the distance between the two edges of the Py electrodes was less than 5 nm, and the Py thickness was greater than 20 nm. This high magnetic field produces a large Zeeman effect in the sandwiched

materials between the two edges of the magnetic thin-film electrodes. The Zeeman splitting energy  $\Delta E_H$  can be expressed by  $2g\mu_B SH$ , where  $g$  is the  $g$ -factor of electrons,  $\mu_B$  is the Bohr magneton ( $58 \mu\text{eV/T}$ ),  $S$  is the spin quantum number, and  $H$  is the magnetic field. Here,  $g$  is almost equal to 2.0 and  $H$  is 5 kOe, as obtained by the above calculation. Because a large spin  $S$  of the order of a few hundred to a thousand has been reported in QDs such as MnAs nanoparticles in a GaAs matrix [24],  $\Delta E_H$  was estimated to be a few 10–100 meV. This large Zeeman splitting produces a large spin-filter effect. Although the stray field in Py-based SQC devices (5 kOe) is almost similar to or slightly smaller than that in Co-based SQC devices (6 kOe) [12], the above estimation reveals that a stray field of 5 kOe is enough high to obtain a large spin filter effect. These experimental and calculated results suggest that Py thin films with a thickness of around 20 nm sandwiched between LSP glasses can be used as electrodes in SQC devices, providing a spin-filter effect, and also our proposed techniques utilizing magnetic thin-film edges will open up new opportunities for the creation of high performance spin devices, such as large magnetoresistance devices and nanoscale spin injectors.

#### **4. Conclusion**

We have investigated the structural and magnetic properties of Py thin films sandwiched between LSP glasses, which can be used in SQC devices. We have successfully demonstrated the formation of LSP-glass/Py/LSP-glass structures with smooth and clear interfaces. The coercivity of Py thin films was drastically enhanced from 0.9 to 103 Oe after thermal pressing at 1.0 MPa. According to the TEM and TED observations, XRD measurements, and theoretical

calculations based on the random anisotropy model, this coercivity enhancement can be explained by the increase in crystal grain size with random magnetic anisotropy. A uniform stray magnetic field was also observed from the Py thin-film edge in the direction perpendicular to the cross section of the LSP-glass/Py/LSP-glass structures. The results of micromagnetic simulation indicated that a high stray field of around 5 kOe was generated when the distance between the two edges of the Py thin-film electrodes was less than 5 nm, and the Py thickness was larger than 20 nm. These experimental and calculated results indicate that Py thin films sandwiched between LSP glasses are useful as the electrodes of SQC devices, where they serve as spin-filter devices.

### **Acknowledgments**

This research was partially supported by Grant-in-Aid for Scientific Research (B) and Challenging Exploratory Research from the Japan Society for the Promotion of Science (JSPS), the Precursory Research for Embryonic Science and Technology program from the Japan Science and Technology Agency (JST), and the Cooperative Research Program of the Network Joint Research Center for Materials and Devices from the Ministry of Education, Culture, Sports, Science and Technology (MEXT). The authors would like to express their sincere appreciation to Prof. Y. Matsuo, N. Kawai, H. Kasa, K. Nakamura, T. Ohta, and M. Takei of Hokkaido University and N. Yamashita of ISUZU GLASS CO., LTD. for their cooperation and helpful discussions.

## References

- [1] G. Binasch, P. Grünberg, F. Saurenbach, W. Zinn, Enhanced magnetoresistance in layered magnetic structures with antiferromagnetic interlayer exchange, *Phys. Rev. B* 39 (1989) 4828–4830.
- [2] M. N. Baibich, J. M. Broto, A. Fert, F. Nguyen, Van Dau, F. Petroff, Giant Magnetoresistance of (001)Fe/(001)Cr Magnetic Superlattices, *Phys. Rev. Lett.* 61 (1988) 2472–2475.
- [3] T. Miyazaki, N. Tezuka, Giant magnetic tunneling effect in Fe/Al<sub>2</sub>O<sub>3</sub>/Fe junction, *J. Magn. Magn. Mater.* 139 (1995) L231–L234.
- [4] J. S. Moodera, L. R. Kinder, T. M. Wong, R. Meservey, Large Magnetoresistance at Room Temperature in Ferromagnetic Thin Film Tunnel Junctions, *Phys. Rev. Lett.* 74 (1995) 3273–3276.
- [5] B. Dieny, V. S. Speriosu, S. S. P. Parkin, B. A. Gurney, D. R. Wilhoit, D. Mauri, Giant magnetoresistance in soft ferromagnetic multilayers, *Phys. Rev. B* 43 (1991) 1297–1300.
- [6] J. S. Moodera, X. Hao, G. A. Gibson, R. Meservey, Electron-Spin Polarization in Tunnel Junctions in Zero Applied Field with Ferromagnetic EuS Barriers, *Phys. Rev. Lett.* 61 (1988) 637–640.
- [7] T. Nagahama, T. S. Santos, J. S. Moodera, Enhanced Magnetotransport at High Bias in Quasimagnetic Tunnel Junctions with EuS Spin-Filter Barriers, *Phys. Rev. Lett.* 99 (2007) 016602-1–016602-4.
- [8] J. S. Moodera, R. Meservey, X. Hao, Variation of the Electron-Spin Polarization in EuSe

Tunnel Junctions from Zero to Near 100% in a Magnetic Field, *Phys. Rev. Lett.* 70 (1993) 853–856.

[9] M. Gajek, M. Bibes, A. Barthélémy, K. Bouzehouane, S. Fusil, M. Varela, J. Fontcuberta, A. Fert, Spin filtering through ferromagnetic BiMnO<sub>3</sub> tunnel barriers, *Phys. Rev. B* 72 (2005) 020406-1–020406-4.

[10] T. Koga, J. Nitta, H. Takayanagi, S. Datta, Spin-Filter Device Based on the Rashba Effect Using a Nonmagnetic Resonant Tunneling Diode, *Phys. Rev. Lett.* 88 (2002) 126601-1–126601-4.

[11] H. Kaiju, H. Kasa, T. Komine, T. Abe, T. Misawa, J. Nishii, Magnetic Properties of Spin Quantum Cross Devices Utilizing Stray Magnetic Fields, *Mater. Res. Soc. Symp. Proc.* 1708 (2014) vv0910-1–vv0910-6.

[12] H. Kaiju, H. Kasa, T. Komine, S. Mori, T. Misawa, T. Abe, and J. Nishii, Co thickness dependence of structural and magnetic properties in spin quantum cross devices utilizing stray magnetic fields, *J. Appl. Phys.* 117 (2015) 17C738-1–17C738-4.

[13] G. Chin, Review of Magnetic Properties of Fe-Ni Alloys, *IEEE Trans. Magn.* 7 (1971) 102–113.

[14] A. Slachter, F. L. Bakker, J-P. Adam, B. J. van Wees, Thermally driven spin injection from a ferromagnet into a non-magnetic metal, *Nat. Phys.* 6 (2010) 879–882.

[15] Y. Fukuma, L. Wang, H. Idzuchi, S. Takahashi, S. Maekawa, Y. Otani, Giant enhancement of spin accumulation and long-distance spin precession in metallic lateral spin valves, *Nat. Mater.* 10 (2011) 527–531.

- [16] P. Tyagi, E. Friebe, C. Baker, Advantages of Prefabricated Tunnel Junction-Based Molecular Spintronics Devices, *NANO* 10 (2015) 1530002-1–1530002-22.
- [17] P. Saravanan, J. H. Hsu, C. L. Tsai, A. K. Singh, P. Alagarsamy, Effect of Ta Underlayer on Thickness-Dependent Magnetic Properties of Ni-Fe Films, *IEEE Trans. Magn.* 51 (2015) 2006604-1–2006604-4.
- [18] P. Thangadurai, Y. Lumelsky, M. S. Silverstein, W. D. Kaplan, TEM specimen preparation of Semiconductor-PMMA-metal interfaces, *Mater. Charact.* 59 (2008) 1623–1629.
- [19] A. Thran, T. Strunskus, V. Zaporozhchenko, F. Faupel, Evidence of noble metal diffusion in polymers at room temperature and its retardation by a chromium barrier, *Appl. Phys. Lett.* 81 (2002) 244–246.
- [20] H. Kaiju, N. Basheer, K. Kondo, A. Ishibashi, Surface Roughness and Magnetic Properties of Ni and Ni<sub>78</sub>Fe<sub>22</sub> Thin Films on Polyethylene Naphthalate Organic Substrates, *IEEE Trans. Magn.* 46 (2010) 1356–1359.
- [21] K. Ohkawa, T. Nakano, S. Baba, Evolution of the Scaling of the Surface Roughness Observed on Sputtered Copper Films with Atomic Force Microscope, *J. Vac. Soc. Jpn.* 45 (2002) 134–137.
- [22] A. Alben, J. J. Becker, M. C. Chi, Random anisotropy in amorphous ferromagnets, *J. Appl. Phys.* 49 (1978) 1653–1658.
- [23] G. Herzer, Grain Size Dependence of Coercivity and Permeability in Nanocrystalline Ferromagnets, *IEEE Trans. Magn.* 26 (1990) 1397–1402.
- [24] P. N. Hai, S. Ohya, M. Tanaka, S. E. Barnes, S. Maekawa, Electromotive force and huge

magnetoresistance in magnetic tunnel junctions, *Nature* 458 (2009) 489–492.

## Figure captions

**Fig. 1.** Cross-sectional TEM images of (a) Py17 and (b) Py86 and high-resolution cross-sectional TEM images of the same specimens of (c) Py17 and (d) Py86. Carbon layers were deposited on the Py thin films for protection.

**Fig. 2.** (a) Surface roughness as a function of film thickness for Py thin films on LSP glasses and (b) scaling properties of the surface roughness for an LSP glass, Py9, Py25, and Py86.

**Fig. 3.** Magnetization curves of (a) Py17 and (b) Py86.

**Fig. 4.** Cross-sectional TEM images of (a) s-Py13 and (b) s-Py78 under thermal pressing at  $P = 1.0$  MPa and high-resolution cross-sectional TEM images of the same specimens of (c) s-Py13 and (d) s-Py78.

**Fig. 5.** Magnetization curves of (a) s-Py13 and (b) s-Py78 using the thermal pressing process at  $P = 1.0$  MPa.

**Fig. 6.** Pressure dependence of the coercivity of Py thin films sandwiched between LSP glasses.

**Fig. 7.** Diffraction patterns of (a) Py17, (b) Py86, (c) s-Py13, and (d) s-Py78.

**Fig. 8.** XRD spectra of Py86 before and after thermal pressing at  $P = 1.0$  MPa.

**Fig. 9.** AFM images of polished cross-sectional surfaces of (a) s-Py13 and (b) s-Py78 and MFM images of the same specimens of (c) s-Py13 and (d) s-Py78.

**Fig. 10.** (a) Structure of an SQC device for the calculation of the stray field between the two edges of Py thin-film electrodes. Calculation results of the stray field in the junction of SQC devices with (b)  $t_{y(z)} = 5$  nm and  $d = 20$  nm, (c)  $t_{y(z)} = 20$  nm and  $d = 20$  nm, and (d)  $t_{y(z)} = 20$

nm and  $d = 5$  nm. (e) The stray field in the center of the junction as a function of the Py thickness.

**Table caption**

**Table 1.** Average crystal grain sizes of Py86 before and after thermal pressing (denoted by  $l_{g,before}$  and  $l_{g,after}$ ).

Crystal plane	(111)	(200)	(220)
$l_{g,before}$	8.5 nm	5.9 nm	5.1 nm
$l_{g,after}$	17.8 nm	14.0 nm	17.1 nm

Table 1. T. Misawa, S. Mori, T. Komine,  
M. Fujioka, J. Nishii, H. Kaiju

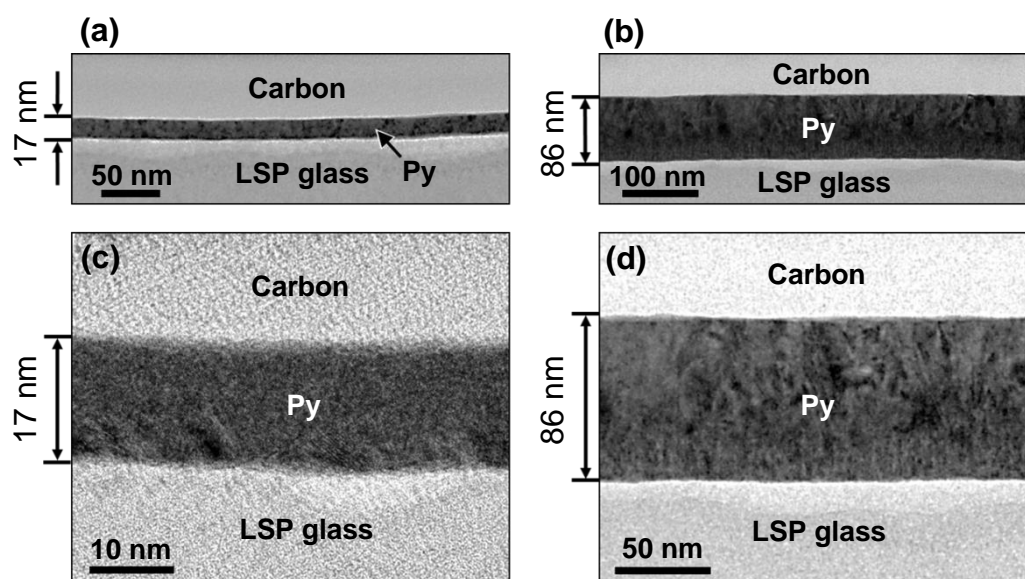


Fig. 1. T. Misawa, S. Mori, T. Komine,  
M. Fujioka, J. Nishii, H. Kaiju

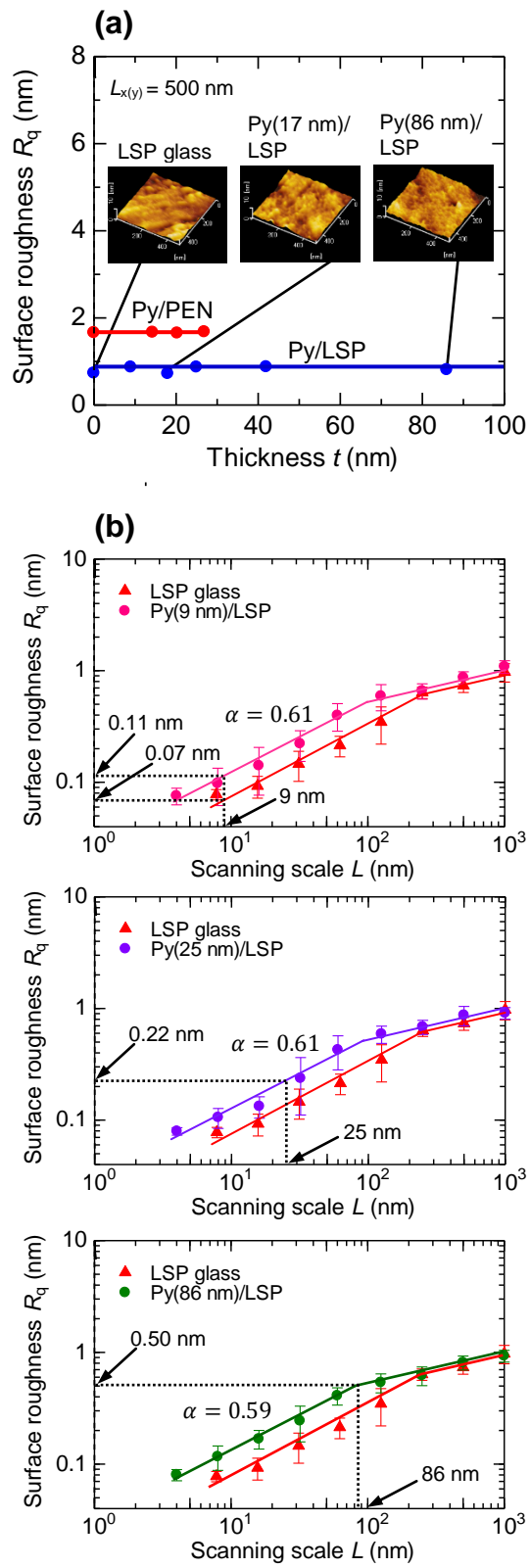


Fig. 2. T. Misawa, S. Mori, T. Komine, M. Fujioka, J. Nishii, H. Kaiju

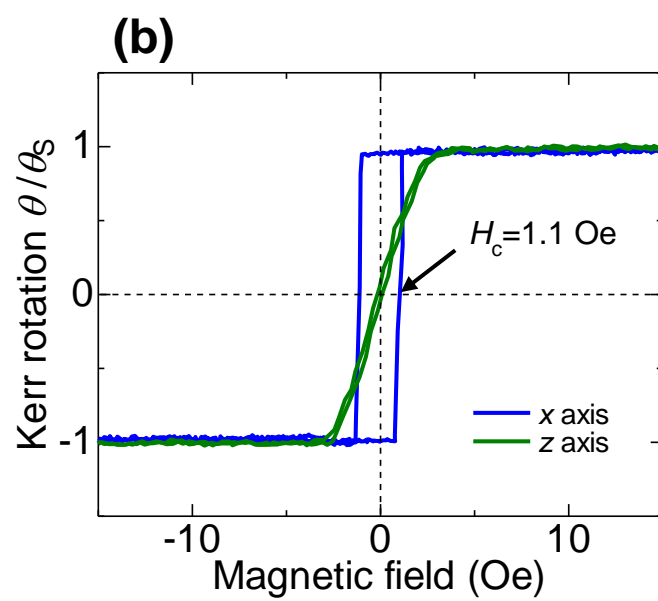
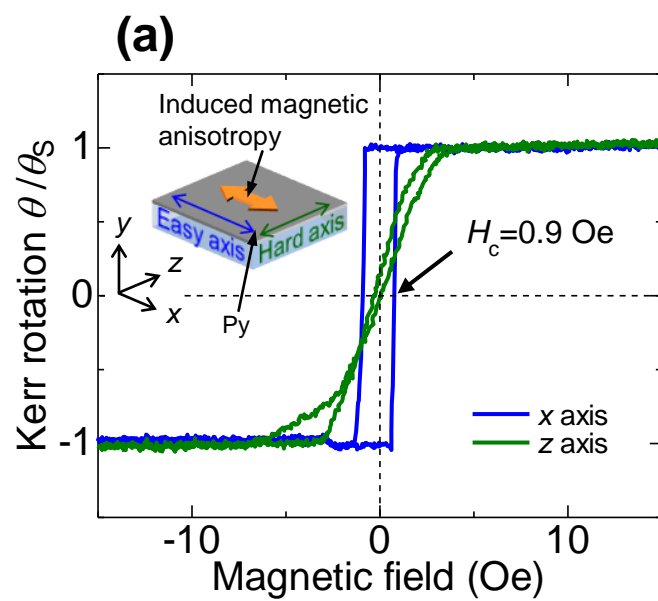


Fig. 3. T. Misawa, S. Mori, T. Komine, M. Fujioka, J. Nishii, H. Kaiju

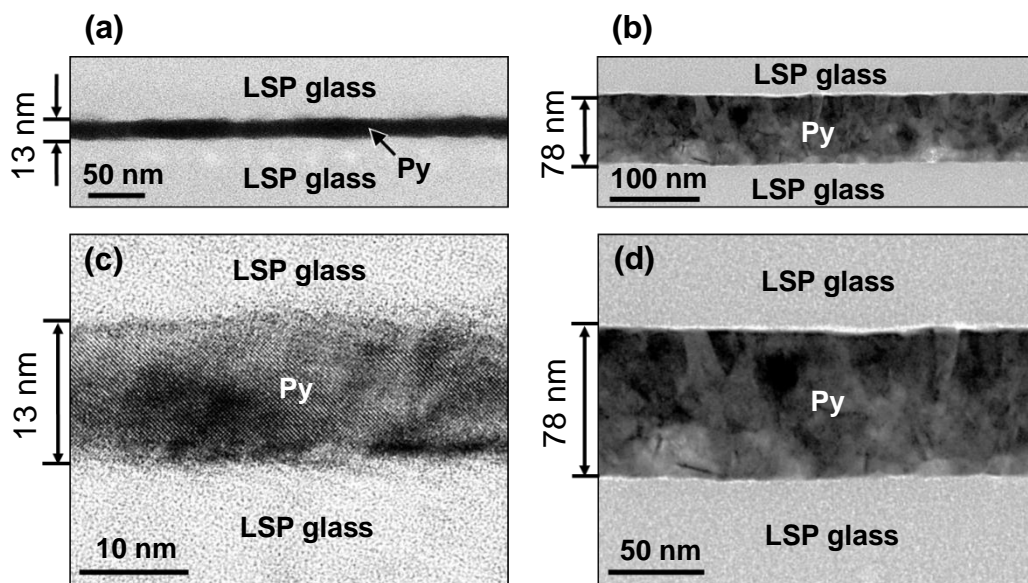


Fig. 4. T. Misawa, S. Mori, T. Komine, M. Fujioka, J. Nishii, H. Kaiju

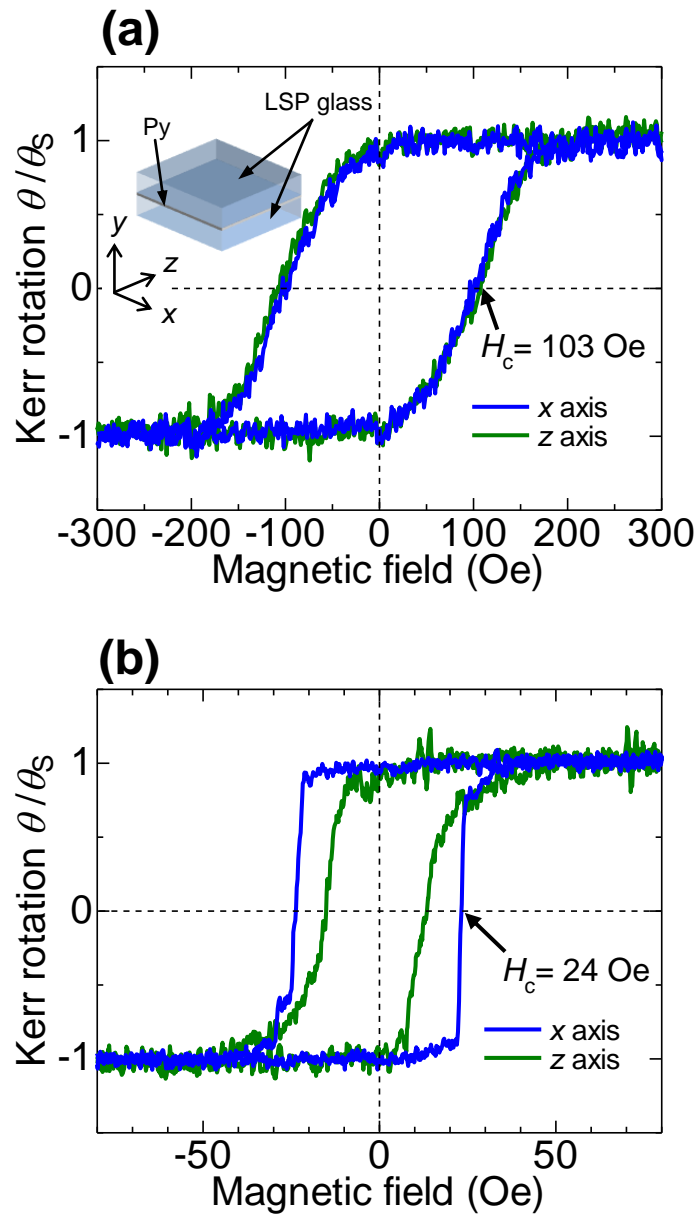


Fig. 5. T. Misawa, S. Mori, T. Komine,  
M. Fujioka, J. Nishii, H. Kaiju

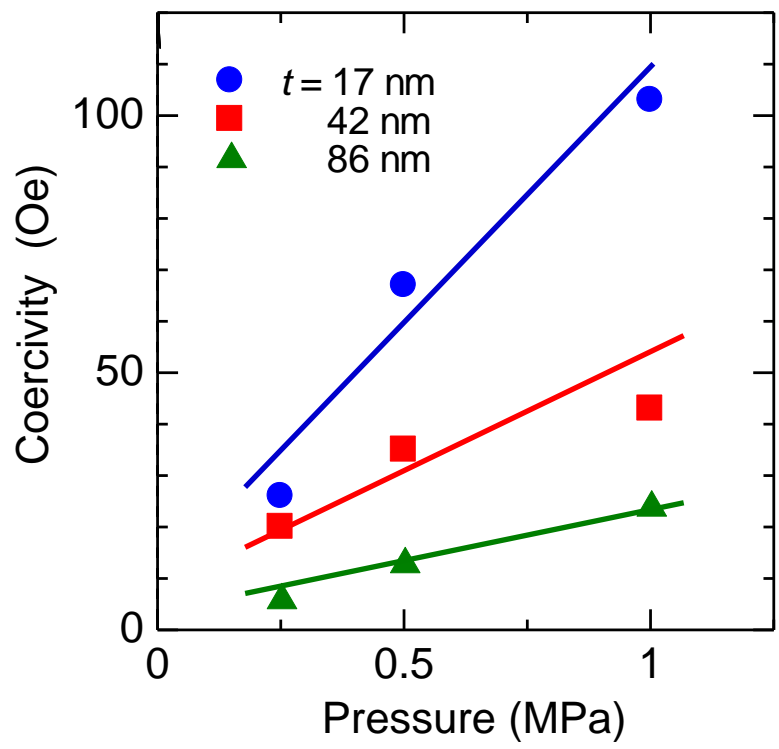


Fig. 6. T. Misawa, S. Mori, T. Komine,  
M. Fujioka, J. Nishii, H. Kaiju

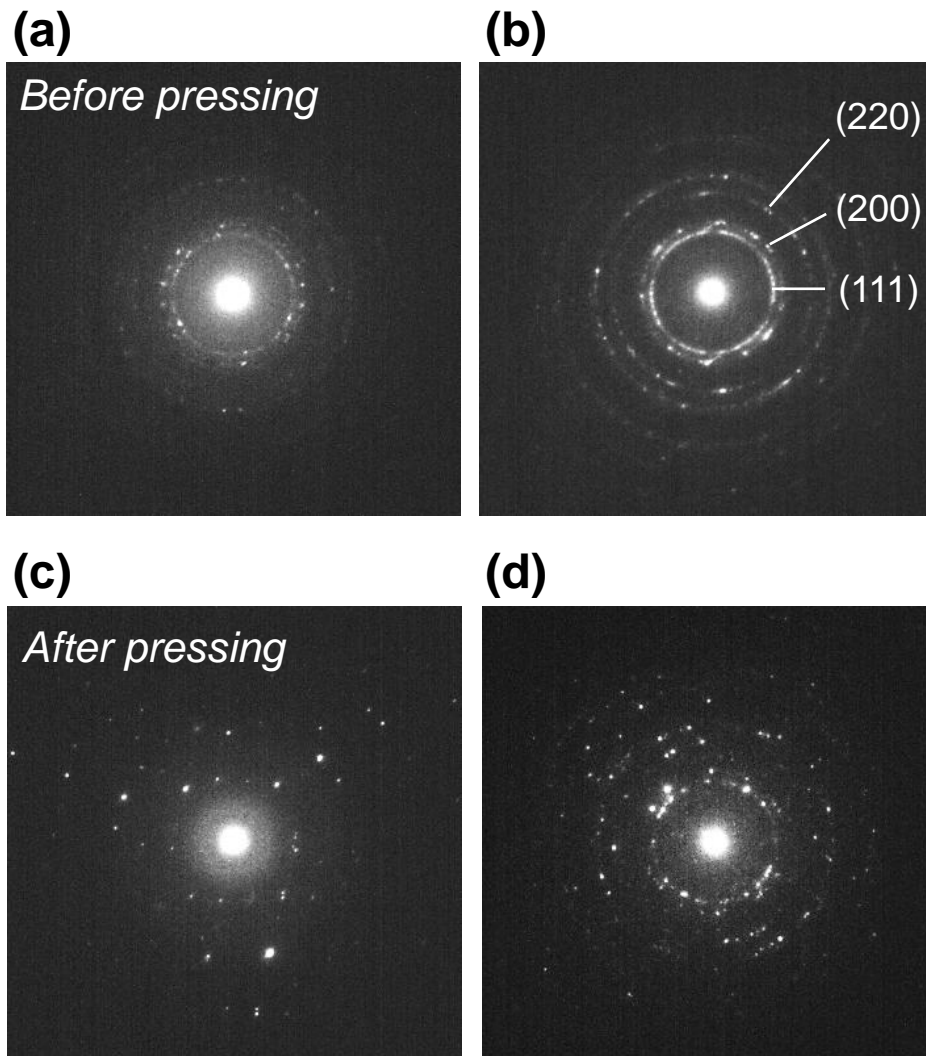


Fig. 7. T. Misawa, S. Mori, T. Komine,  
M. Fujioka, J. Nishii, H. Kaiju

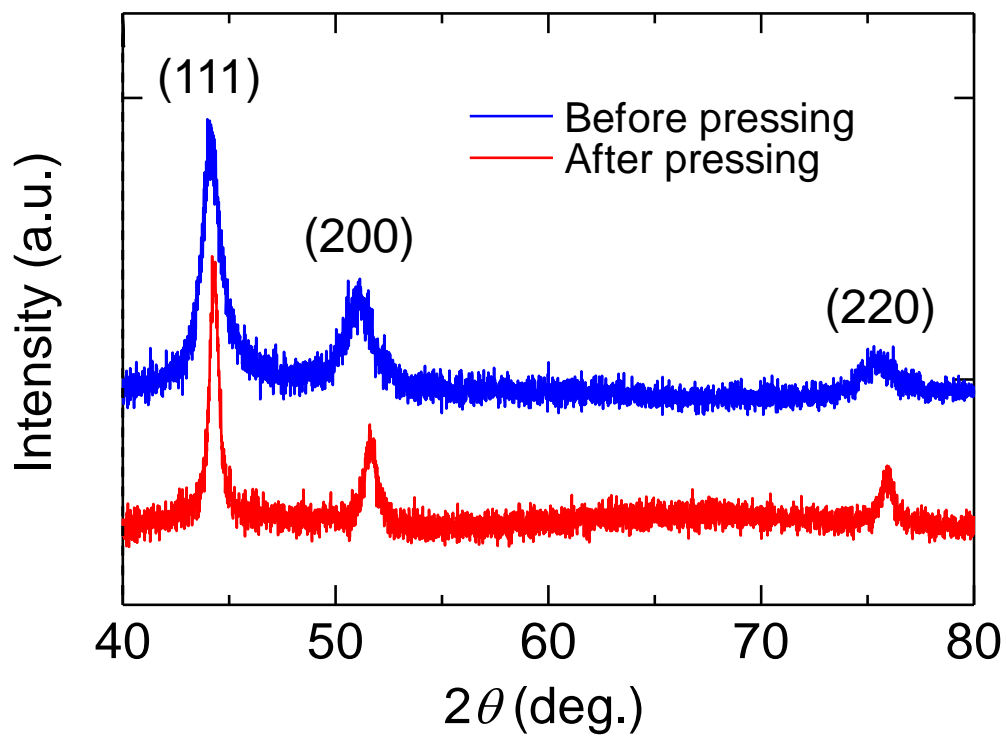
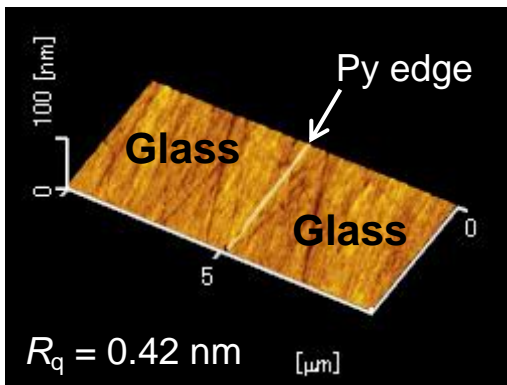
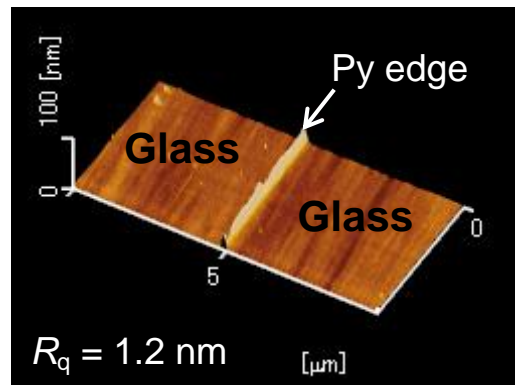


Fig. 8. T. Misawa, S. Mori, T. Komine,  
M. Fujioka, J. Nishii, H. Kaiju

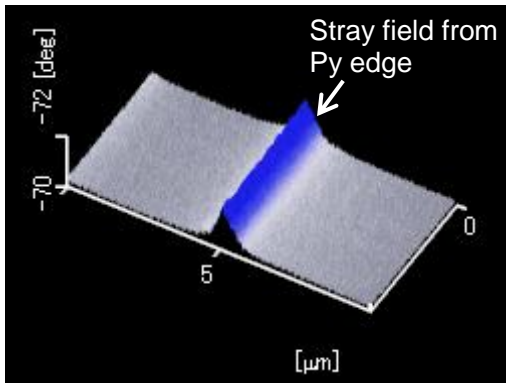
(a)



(b)



(c)



(d)

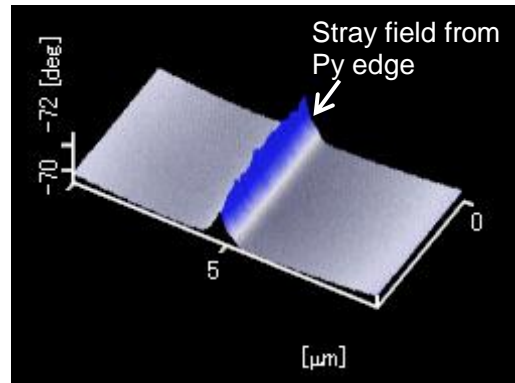


Fig. 9. T. Misawa, S. Mori, T. Komine, M. Fujioka, J. Nishii, H. Kaiju

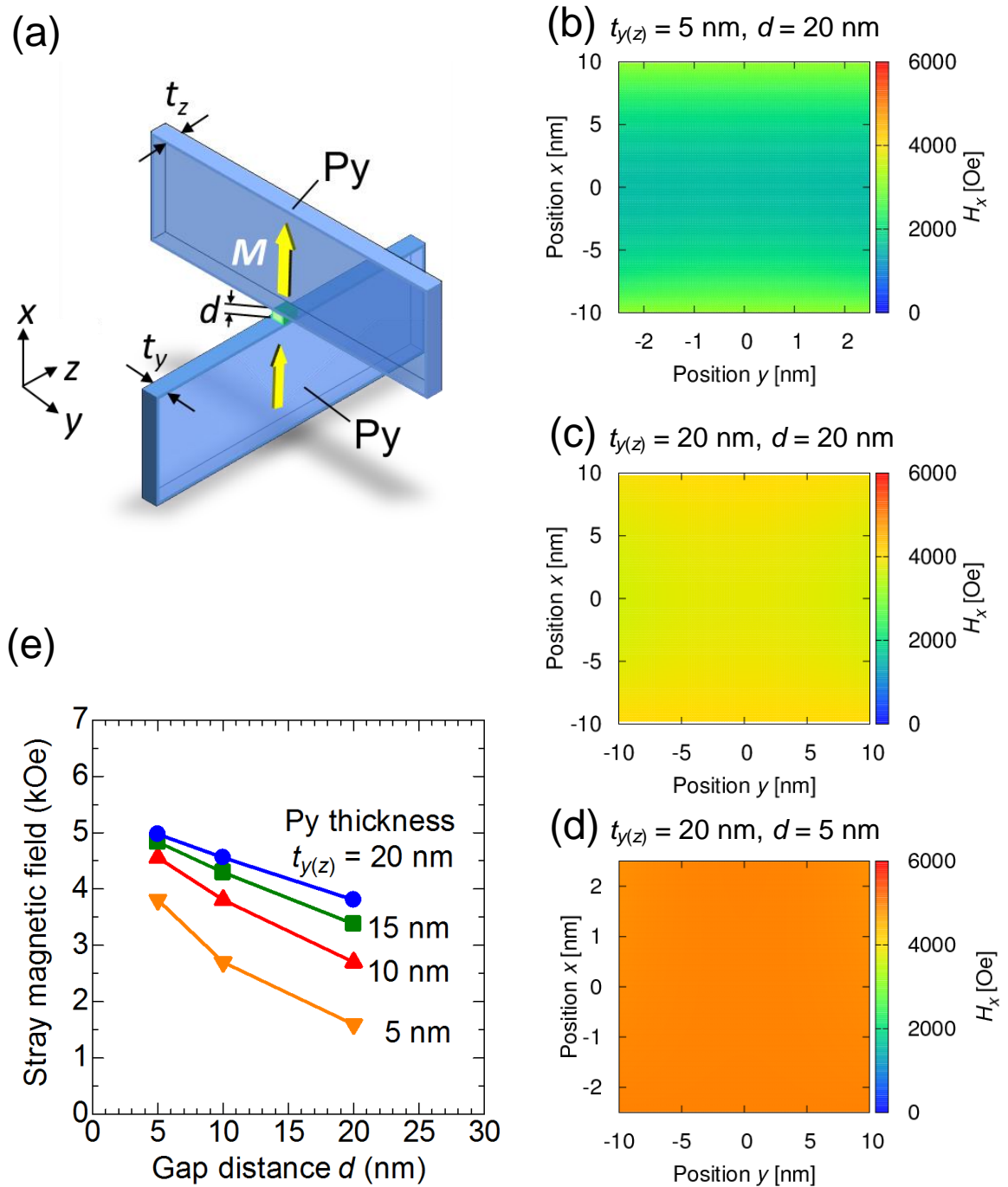


Fig. 10. T. Misawa, S. Mori, T. Komine, M. Fujioka, J. Nishii, H. Kaiju